Materials Advances

ROYAL SOCIETY OF CHEMISTRY

PAPER

View Article Online
View Journal | View Issue

Cite this: *Mater. Adv.*, 2026, 7, 338

Enhanced adsorption of methylene blue (MB) dye by the MoS_2/ZIF-8 composite: isotherm and kinetics studies

Rofaida F. H. Darweesh,[a] Remon M. Zaki,[ad] Aldoshy Mahdy[b] and Abdelaal S. A. Ahmed *[c]

In this study, a zeolitic imidazolate framework (ZIF-8) loaded with molybdenum disulfide (MoS_2) was prepared *via* a hydrothermal method. The as-prepared MoS_2/ZIF-8 composite displayed a mesoporous structure with a BET surface area of 19.13 m^2 g^{-1} and a mean pore diameter of 9.33 nm. The as-prepared ZIF-8 and MoS_2/ZIF-8 composite were utilized as adsorbents for cationic dye from aqueous solution, and methylene blue (MB) dye was used as a pollutant model. The effects of pH, contact time, initial dye concentrations, adsorbent doses, and temperature on the adsorption efficiency were investigated. The adsorption study confirmed that the MoS_2/ZIF-8 composite displayed higher adsorption capacity toward MB dye than that achieved with pristine ZIF-8. Moreover, the adsorption of MB dye onto ZIF-8 and the MoS_2/ZIF-8 composite is an endothermic process. The adsorption kinetics confirmed that the adsorption of MB onto ZIF-8 and the MoS_2/ZIF-8 composite fit the pseudo-second-order models, and the adsorption isotherm agreed with the Langmuir isotherm models, which confirms the chemical adsorption process. The estimated maximum adsorption capacities of ZIF-8 and the MoS_2/ZIF-8 composite were 68.02 and 85.52 mg g^{-1}, respectively. Thermodynamic analysis determined the process to be spontaneous, endothermic, and followed by enhancement of disorder at the solid–liquid interface. Mechanistic interpretations suggest MB adsorption to be mediated by electrostatic attraction, chemisorption at active sites, and physisorption *via* van der Waals forces. The MoS_2/ZIF-8 composite is thus a highly effective and recyclable adsorbent for desorption of cationic dye from wastewater.

Received 12th June 2025,
Accepted 29th October 2025

DOI: 10.1039/d5ma00636h

rsc.li/materials-advances

1. Introduction

The rising global population, coupled with the limited availability of freshwater, presents a major environmental challenge. As water consumption continues to increase, vast amounts of both organic and inorganic pollutants such as pesticides, heavy metals, detergents, and dyes have significantly polluted various water sources.[1] Over the years, numerous industries, including the paper, food, pharmaceuticals, tanning, textiles, and pigmentation industries, have been responsible for producing substantial volumes of colored effluents. Each year, over 1.6 million tons of dyes are produced, with 10–15% of them being released into wastewater.[2] Dyeing effluents often have high chemical and biochemical oxygen demand (COD and BOD) levels and strong color intensity. Releasing untreated water into the environment is a significant challenge due to its toxicity and potential carcinogenic effects. Furthermore, many aromatic dyes are non-biodegradable and can cause both short-term and long-term harm to aquatic life and humans. These dyes are toxic, stable under chemical and heat conditions, and resistant to biodegradation. Usually, these dyes are harmful to the aquatic ecosystem by lowering the aesthetic value of water features and obstructing light penetration. These dyes also cause human renal, liver, and nervous system dysfunction. Therefore, it is crucial to develop effective methods to remove synthetic dyes from water.[3] To date, these contaminants have been removed from wastewater using a variety of methods, including displacement, electrochemical, coagulation, ozonation, nano filtering, reverse osmosis, advanced oxidation processes, and photocatalytic degradation.[4–9] However, these methods have several drawbacks, such as low recovery rates, limited selectivity, and high operational and maintenance costs. Adsorption is a promising technique for removing dyes from aqueous solutions due to its high efficiency, simplicity, cost-effectiveness, absence of by-products, and rapid processing time.[10,11] The primary challenge in the adsorption process is the morphologies of the

[a] *Environment Science Department, Faculty of Sugar and Integrated Industries Technology, Assiut University, 71516, Egypt*
[b] *Zoology Department, Faculty of Science, Al-Azhar University, Assiut, 71524, Egypt*
[c] *Chemistry Department, Faculty of Science, Al-Azhar University, Assiut, 71524, Egypt. E-mail: abdelaalsaiyd@gmail.com, abdelaalsaiyd@azhar.edu.eg*
[d] *Chemistry Department, Faculty of Science, Assiut University, Assiut 71516, Egypt*

adsorbent materials, which are essential to the overall adsorption performance.[12,13] In recent decades, a lot of materials have been used as effective adsorbent materials toward organic dyes such as carbons,[4,14] metal oxides,[15,16] and agricultural by-products.[17] Metal–organic frameworks (MOFs) have garnered significant interest as promising crystalline materials, known for their unique three-dimensional (3D) porous nanostructures. These materials are made up of organic–inorganic composites, combining metal ions and organic linkers.[18] Due to their exceptional properties such as high surface area, ordered structures, and excellent chemical and thermal stabilities, MOFs have attracted much interest for various applications such as generation of hydrogen.[19] CO_2 uptake,[20] counter electrodes for solar cells[21,22] *etc.*

In terms of environmental issues, MOF-based materials have demonstrated excellent removal efficacy against hazardous dyes during day removal.[23,24] Recently, zeolitic–imidazolium frameworks (ZIFs), a well-known category of MOFs, have attracted great attention because of their exceptional chemical and physical properties, as well as their high surface area.[25] Nevertheless, pure ZIF-8 often has a smaller size and poorer solvent tolerance, which limits its adsorption effectiveness.[26] To overcome these drawbacks, numerous ZIF-8-based composites have been developed by mixing it with other materials to enhance adsorption performance.[27–29] For instance, a ZIF-8@ZIF-67 bimetallic composite showed a strong adsorption affinity for rhodamine B (RhB), achieving a maximum adsorption capacity of 143.26 mg g^{-1}. This capacity was significantly higher than that of pure ZIF-8 (56.40 mg g^{-1}) and ZIF-67 (81.63 mg g^{-1}).[30] In another study, the core–shell-structured ZIF-8@ZIF-67 with a BET surface area of 1518.75 m^2 g^{-1} was successfully used as an adsorbent for removing Direct Blue-86, Reactive Yellow, and Congo Red dyes from aqueous solutions.[31] Additionally, metal oxides are employed to increase the adsorptive capacity of ZIF-8. For example, D. Tuncel and A. N. Ökte reported that the adsorption capability of the ZnO–ZIF-8 composite toward MO and MB dyes is greater than that of pure ZIF-8.[32] Two-dimensional (2D) materials significantly enhanced the adsorption performance of ZIF-8 toward organic dyes.[33] For example, our recent study reported that ZIF-8@graphene oxide (GO) composites prepared at room temperature showed excellent adsorption capacity toward MB and MO dyes.[27] The estimated maximum adsorption capacities of the ZIF-8@0.5GO composite toward MB and MO are 87.39 and 82.78 mg g^{-1}, which are both much higher than that achieved with pure ZIF-8 and very close to those obtained by pure GO. Among 2D materials, molybdenum disulfide (MoS_2) displayed a promising ability in various applications such as electrocatalysts in hydrogen evolution reaction (HER)[34,35] and energy conversion.[22,36–38] Therefore, combining MoS_2 with ZIF-8 is expected to enhance the adsorption capacity.

Therefore, in the current study, MoS_2 layers were blended with ZIF-8 crystals *via* hydrothermal synthesis to synthesize a MoS_2/ZIF-8 composite material. The synthesized material was used as an efficient adsorbent to remove methylene blue (MB) – a commonly used cationic dye that is highly stable, toxic, and frequently found in textile wastewater – from aqueous solutions. The experiment showed that preloading MoS_2 significantly enhanced the adsorption ability of ZIF-8 towards dye. Our work opens the way for developing further ZIF-based materials for the removal of various organic pollutants from wastewater. The main aim of this work is to synthesize and characterize a novel MoS_2/ZIF-8 composite and assess its performance in removing methylene blue dye from water, while correlating its structure and surface properties with adsorption efficiency.

2. Experimental

2.1. Materials

All chemicals used in this study were of analytical grade. Zinc acetate dihydrate ($(CH_3COO)_2Zn{\cdot}2H_2O$), 2-methyl imidazole ($C_4H_6N_2$), thiourea ($CH_4N_2S$), ammonium molybdate ($(NH_4)_6MO_7O_{24}$), methylene blue ($C_{16}H_{18}N_3SCl$), hydrochloric acid (HCl, 37%), and sodium hydroxide (NaOH, >98%) were from Alpha Chemika, India. All reagents used were of analytical purity.

2.2. Preparation of ZIF-8 and the MoS_2/ZIF-8 composite

Crystalline pure ZIF-8 was prepared as described in a previous literature report.[27] An aqueous solution of zinc acetate (0.22 g in 10 mL distilled water) was gradually added into an aqueous solution of 2-methylimidazole (2 g in 70 mL distilled water) slowly under magnetic stirring for 1 h at room temperature. The white precipitate thus obtained was collected by centrifugation at 4500 rpm, washed several times with distilled water, and dried for 12 h at 100 °C. The powdered ZIF-8 crystals were then ground into powder and utilized for further studies. The MoS_2/ZIF-8 composite was synthesized following our previous procedure. In brief, 0.10 g of ZIF-8 was dispersed in 30 mL of distilled water, after which aqueous solutions of thiourea (1.25 g in 25 mL) and ammonium molybdate (0.13 g in 25 mL) were slowly added under stirring for 1 h at room temperature. The mixture was then transferred into a Teflon-lined autoclave and heated at 180 °C for 24 h. After cooling, the product was collected by centrifugation at 3000 rpm, repeatedly washed with distilled water, dried at 90 °C for 12 h, and ground into a fine powder. The Mo : S molar ratio was maintained at approximately 1 : 4, which is reported to promote uniform nucleation and growth of MoS_2 nanosheets on porous supports. The selected hydrothermal conditions (180 °C, 24 h) were chosen to enable complete thiourea decomposition, efficient reduction of Mo(VI), and the formation of well-crystallized MoS_2 while preserving the structural integrity of ZIF-8. These optimized ratios and parameters play a crucial role in determining the composite's crystallinity, interfacial interactions, and overall adsorption performance.

2.3. Characterization

Structural and morphological characterization of the synthesized ZIF-8 and MoS_2/ZIF-8 composites was carried out using a combination of complementary techniques to study their structural, morphological, and surface characteristics, all of which

are directly related to the study of their adsorption capacity. FTIR was used to determine the functional groups present in the synthesized materials to confirm the presence of coordination bonds in the organic linker and metal centers. XRD patterns were recorded on a Bruker D8 Advance diffractometer with monochromatized Cu-Kα radiation source (λ = 1.5406 Å) at a scanning range of 2θ = 5–80° and 0.02° step size to verify the crystalline structure and phase composition of the materials. Nitrogen adsorption–desorption isotherms were measured at 77 K by means of a Micromeritics ASAP-2020 analyzer. The specific surface area was obtained from the Brunauer–Emmett–Teller (BET) equation, and the pore size distribution was obtained using the Barrett–Joyner–Halenda (BJH) model. These surface textural analyses were used to correlate the surface area and pore characteristics with the adsorption performance of the composite. Particle size distribution and surface charge were determined on a Zeta Sizer Nano ZS90 (Malvern Instruments Ltd, UK) at 25 °C. The morphology of the resulting materials was examined by field emission scanning electron microscopy (FE-SEM, JSM-6610, JEOL, Japan) along with energy-dispersive X-ray spectroscopy (EDX) carried out at 20 kV, and data on surface morphology as well as elemental composition were obtained. Transmission electron microscopy (TEM) images were obtained from a JEM-2100F field emission microscope (JEOL Ltd, Japan) at an accelerating voltage of 200 kV, to further characterize the inner nanostructure and to confirm the successful deposition of MoS_2 layers on the ZIF-8 framework. An ultraviolet-visible (UV-Vis, Nicolet Evolution 300, Cany Precision Instruments Co., Ltd, China) spectrophotometer was used to determine the residual concentration of methylene blue (MB) dye at the wavelength of absorption maximum λ_{max} = 664 nm. The combination of such characterization techniques provided comprehensive information on the physicochemical nature of materials, enabling correlation between their structural attributes (*e.g.*, crystallinity, surface area, and surface charge) and adsorption activity against MB dye.

2.4. Adsorption study

The experimental conditions adopted were chosen based on previous literature to ensure scientific comparability and consistency. Specifically, the MB concentration ranges (5–200 mg L^{-1}) are commonly employed to simulate the general concentrations of dyes in wastewaters and to examine adsorption for low and high levels of pollutants.[39] A range of adsorbent dosage (0.01–0.10 g) has been widely reported in batch adsorption studies since it provides sufficient active surface sites without overdosing.[4,40] The range of pH tested (3–10) covers environmentally relevant acidic to alkaline conditions and allows examination of the effect of electrostatic interaction between MB cations and adsorbent surface.[27,41] The pH of dye solutions was adjusted by 0.10 M HCl and 0.10 M NaOH aqueous solutions. Contact time up to 120 min is generally sufficient for the development of dye–adsorbent adsorption equilibrium,[42] while the temperature range adopted (30–70 °C) not only simulates ambient conditions but also elevated industrial effluent temperatures, with the provision for thermodynamic analysis of adsorption.[43] These ranges were thus selected below to provide a balanced and science-laden evaluation of ZIF-8 and MoS_2/ZIF-8 composite adsorption performance. After the desired time, the remaining concentration of the MB dye was measured using a UV-visible spectrophotometer at a wavelength of 664 nm.[27,44] The removal percentage (R%) and the adsorption capacity (q_e; mg g^{-1}) of the MB dye were determined using eqn (1) and (2), respectively.

$$R\ (\%) = \frac{C_0 - C_e}{C_0} \times 100 \quad (1)$$

$$q_e = \frac{(C_0 - C_e)}{M} V \quad (2)$$

where C_0 and C_e are the initial and final MB dye concentrations (mg L^{-1}), respectively, V is the volume (L), and M is the mass of the adsorbent (g).

3. Results and discussion

3.1. Characterization of the structure and morphology

The structural features of the as-synthesized ZIF-8 and the MoS_2/ZIF-8 composite were identified by XRD (Fig. 1a). The diffraction pattern of ZIF-8 exhibited a series of well-defined peaks at 2θ = 7.4°, 10.4°, 12.7°, 14.7°, 16.4°, 18.0°, 22.1°, 24.5°, 26.7°, and 29.6°, respectively, corresponding to the (011), (002), (112), (022), (013), (222), (114), (233), (134), and (044) planes, respectively, similar to the typical sodalite-type crystalline structure of ZIF-8.[21,45] For the composite of MoS_2/ZIF-8, four broad diffraction peaks were observed at 2θ = 28.6°, 32.7°, 46.3°, and 56°, indexed to the (100), (102), (006), and (110) planes of hexagonal 2H-MoS_2 (JCPDS 37-1492).[46] ZIF-8 reflection intensity was greatly reduced but not completely removed, indicating that MoS_2 nanosheets have grown well on the ZIF-8 surface, covering partially its diffraction signals. This points towards the formation of a highly integrated hybrid with few-layered MoS_2 of relatively poor crystallinity.[47,48]

The FT-IR spectra of ZIF-8 and MoS_2/ZIF-8 are presented in Fig. 1b. For the ZIF-8 material, characteristic vibrational modes at 1675 and 1585 cm^{-1} correspond to the C=C and C=N stretching for the imidazole ring, while peaks at 3000 and 2990 cm^{-1} correspond to aromatic and aliphatic C–H stretching.[49,50] The FTIR spectrum of the MoS_2/ZIF-8 composite exhibited additional peaks at ~2100, 1650, 1390, and 1140 cm^{-1} attributed to pure MoS_2.[46] The typical Mo–S stretching vibration band observed at ~470–480 cm^{-1} is additional confirmation for the presence of MoS_2. The decrease in intensity of bands characteristic to ZIF-8 in the composite is a sign of strong interfacial interaction and successful coating of MoS_2 onto ZIF-8 particles.

The surface area and porosity of the samples were determined through nitrogen adsorption–desorption isotherms (Fig. 1c). ZIF-8 powder exhibited a Type I isotherm, characteristic of microporous solids, whereas the MoS_2/ZIF-8 composite exhibited a Type IV isotherm with an H3 hysteresis loop, characteristic of mesoporous solids.[51] The pore size distribution curve (Fig. 1d) clearly depicted a dominant mesoporous structure in the composite. Brunauer–Emmett–Teller (BET)

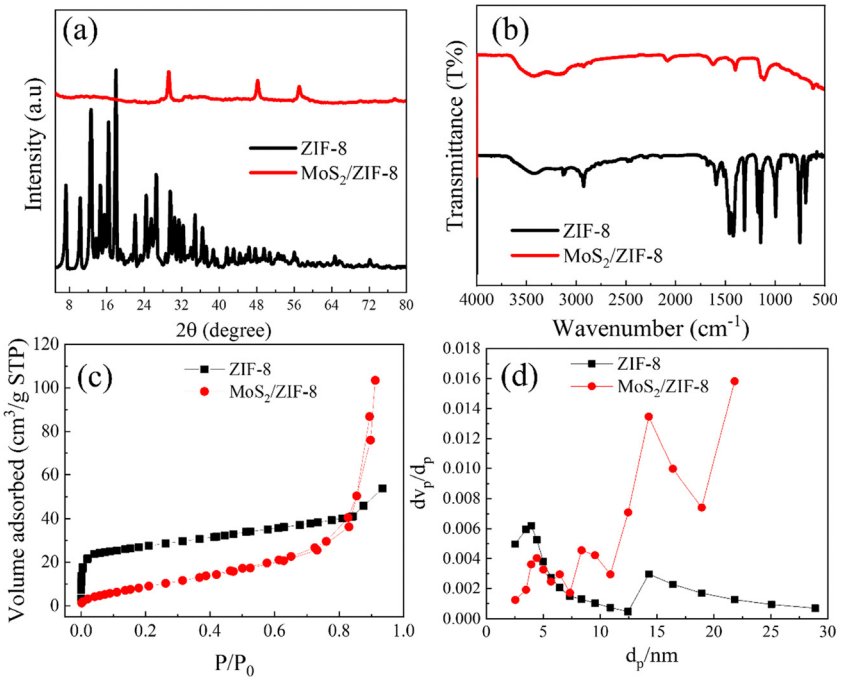

Fig. 1 (a) XRD pattern, (b) FT-IR spectra, (c) nitrogen adsorption–desorption isotherms, and (d) pore size distribution of ZIF-8 and the MoS_2/ZIF-8 composite.

surface area and pore volume of MoS_2/ZIF-8 and ZIF-8 were 41.20 m^2 g^{-1} and 19.13 m^2 g^{-1}, respectively, with average pore diameters of 15.55 and 9.33 nm. A decrease in surface area after MoS_2 deposition reflects partial pore blockage by MoS_2 nanosheets.

The morphology of the as-prepared materials was examined using SEM (Fig. 2). ZIF-8 exhibited uniform rhombic dodecahedral particles with approximate dimensions of around 450 nm (Fig. 2a and b). After the introduction of MoS_2, the obtained MoS_2/ZIF-8 composite (Fig. 2c and d) displayed that the MoS_2 is

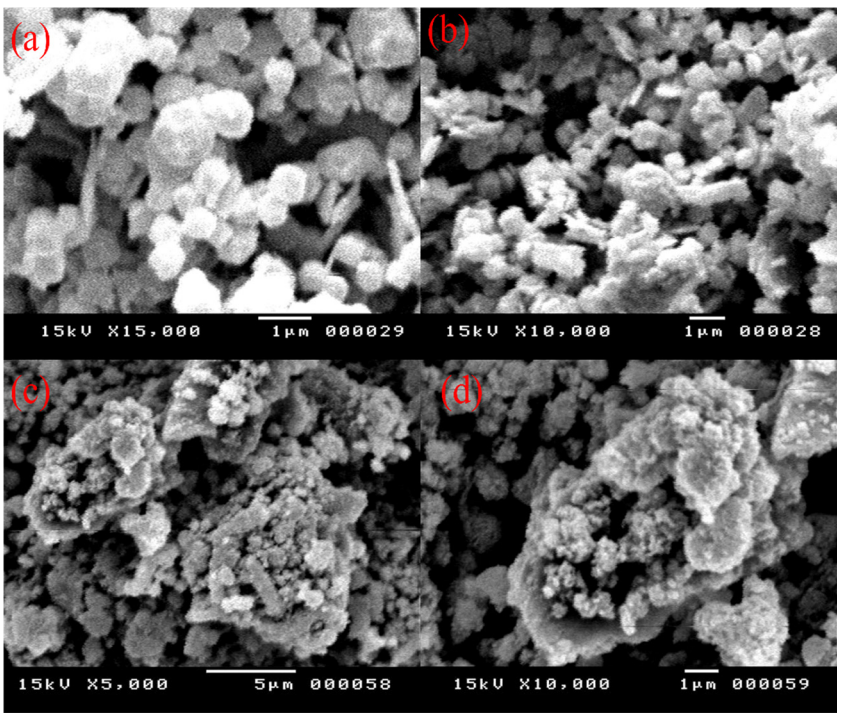

Fig. 2 SEM of (a) and (b) ZIF-8 and (c) and (d) the MoS_2/ZIF-8 composite.

homogeneously grown on the surface of ZIF-8 forming the MoS_2/ZIF-8 composite. This kind of core–shell structure is very beneficial for preventing MoS_2 sheet agglomeration which is important for enhancing the surface area and the overall adsorption performance.

Elemental mapping and analysis (Fig. 3a) verified the homogeneous distribution of Zn, Mo, S, and O elements throughout the composite. The EDX spectrum (Fig. 3b) gave weight percentages of Zn (41.7%), Mo (18.1%), S (28.6%), and O (3.0%). Atomic ratios calculated (Zn : Mo : S $\approx$ 1.0 : 0.43 : 0.95) are in accordance with the expected stoichiometry, confirming successful loading of MoS_2 onto the ZIF-8 structure.

TEM images of the ZIF-8 and MoS_2/ZIF-8 composite are shown in Fig. 4. The TEM image of ZIF-8 (Fig. 4a and b) reveals a clear uniform rhombic dodecahedral structure. On the other hand, TEM images of the MoS_2/ZIF-8 composite (Fig. 4c and d) revealed that the ultrathin MoS_2 nanosheets homogeneously covered the surface of ZIF-8, which is strong evidence for the formation of the MoS_2/ZIF-8 composite.[52] Combining XRD, SEM, and TEM analysis demonstrates that MoS_2 nanosheets were successfully grown onto the surface of ZIF-8 to form MoS_2/ZIF-8 composites.

3.2. Adsorption study

3.2.1. The point of zero charge (pH_{PZC}) and effect of pH. The zero point of charge (pH_pzc) of ZIF-8 and the MoS_2/ZIF-8 composite was studied *via* zeta potential analysis to determine their surface charge characteristics.[53] From Fig. 5, ZIF-8 and MoS_2/ZIF-8 exhibit a neutral pH zeta potential value of +5.54 and −19.8 mV, respectively, with estimated pH_pzc values of 8.1 and 5.9. The composite surface would thus be negatively charged when pH > pH_pzc, facilitating electrostatic attraction with cationic MB^+ molecules.[54]

pH influence on MB adsorption was explored in the range 3–10 by adjusting the pH value using 0.10 M HCl and 0.10 M NaOH. For every experiment, 0.10 g of adsorbent and 40 mL of 30 mg L^{-1} dye solution were shaken for 120 min at 25 °C. From Fig. 6, the maximum MB removal occurred near neutral pH, 93.7% for ZIF-8 at pH 7 and 97.6% for MoS_2/ZIF-8 at pH 6. The higher uptakes at pH > pH_pzc are attributed to favorable

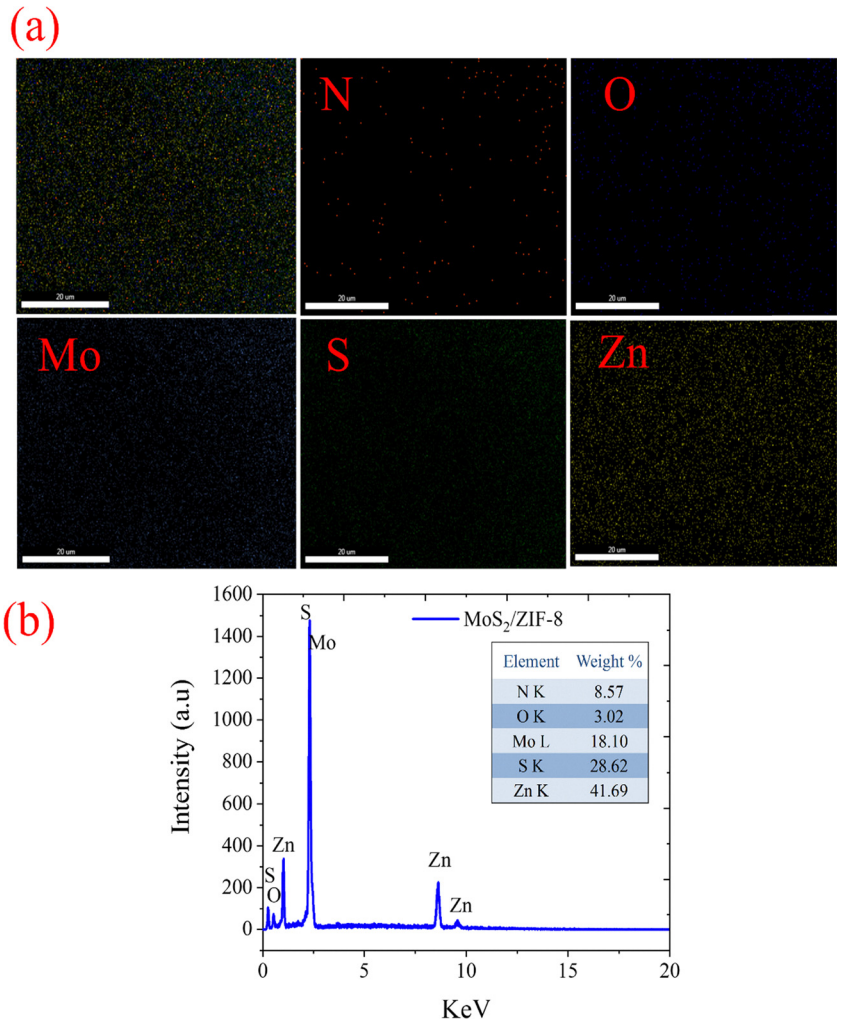

Fig. 3 (a) EDX-mapping and (b) EDX-line for the MoS_2/ZIF-8 composite.

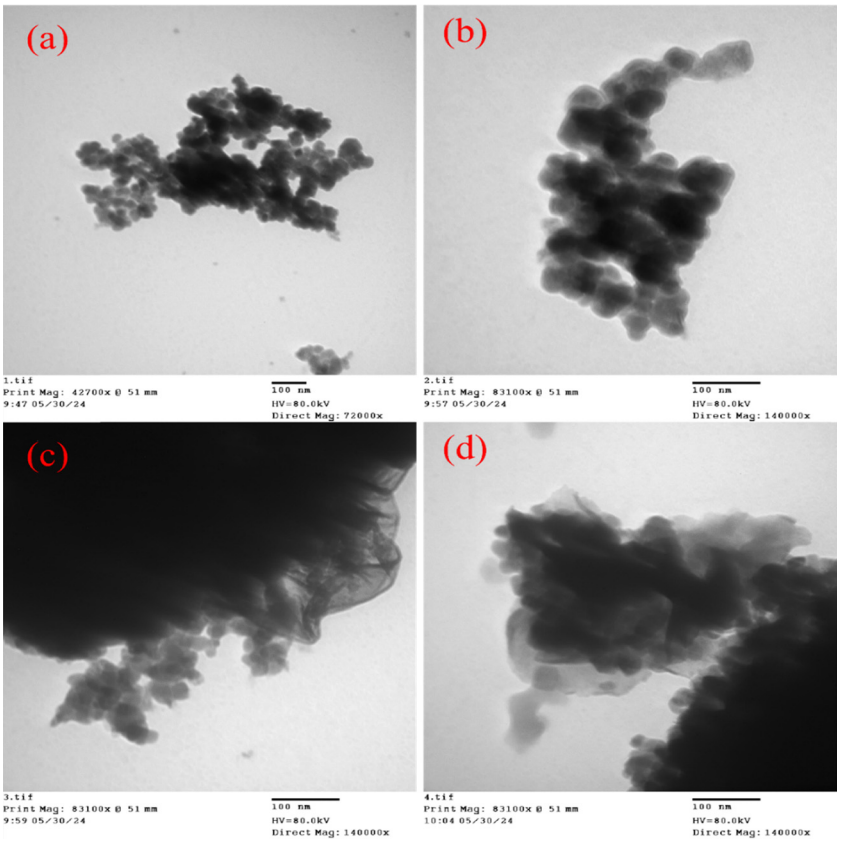

Fig. 4 TEM of (a) and (b) ZIF-8 and (c) and (d) the MoS_2/ZIF-8 composite.

electrostatic interaction between MB^+ and the negatively charged adsorbent surface as previously documented.[27,55]

3.2.2. Effect of contact time. The contact time between the absorbent and adsorbate is crucial for developing wastewater treatment systems.[43] Thus, the impact of contact time on the adsorption efficiency of MB dye onto ZIF-8 and the MoS_2/ZIF-8 composite was examined by stirring dye solutions with an initial concentration of 30 mg L^{-1} and adjusting the acidity of the dye solutions to a pH of 6 and 7 for the MoS_2/ZIF-8 composite and ZIF-8, respectively. To each 40 mL dye solution, 0.1 g of absorbent was added and agitated for durations ranging from 2 to 120 min at 25 °C. Fig. 7a showed that by increasing the contact time from 2 to 120 min, the elimination percentage of MB by ZIF-8 gradually increased from 86.5 to 93.7%, and from 88 to 97.6% by the MoS_2/ZIF-8 composite. The increased adsorption during the early stage (up to 90 min) can be attributed to more vacant adsorption sites. The dye molecule interactions with the adsorbent led to an adsorption plateau, and the bulk phase became more repulsive.[56]

3.2.3. Effect of adsorbent amount. The adsorbent doses play an essential role in avoiding the waste of adsorbent materials after reaching equilibrium.[4,57] In this study, various weights of adsorbent ranging from 0.01 to 0.10 g were mixed separately with a 40 mL MB dye solution with an initial concentration of 30 mg L^{-1}. The acidity of the dye solutions was adjusted to a pH of 7.2 for ZIF-8 and 6.2 for the MoS_2/ZIF-8 composite. All mixtures were stirred for 120 min at room temperature. As shown in Fig. 7b, increasing the weight of adsorbents from 0.01 to 0.10 g resulted in a progressive increase in MB dye removal. This was attributed to more active sites capable of interacting with dye molecules.[58,59]

3.2.4. Adsorption capacity. The adsorption capacity of ZIF-8 and the MoS_2/ZIF-8 composite was determined at different MB initial concentrations. The obtained data are presented in Fig. 8. Typically, 0.10 g of adsorbent was stirred with 40 mL of MB dye with different concentrations ranging from 5 mg L^{-1} to 250 mg L^{-1}, the pH value of all dye solutions was adjusted to 7.2 for ZIF-8 and 6.2 for the MoS_2/ZIF-8 composite and the mixture was stirred for 120 min at 20 °C. We can observe that the adsorption capacity of both adsorbent materials is enhanced by increasing the initial concentration, followed by a slight increase, and finally a barely noticeable increase. The adsorption capacity increased from 1.07 to 68.02 mg g^{-1} for ZIF-8 and from 2.62 to 85.52 mg g^{-1} for the MoS_2/ZIF-8 composite by increasing the initial concentration from 5 to 250 mg L^{-1}. This is mostly explained by the increase in repulsion forces between the MB molecules on the surface of the adsorbent and the bulk phase following initial adsorption.[60,61] It was observed that for the previous result at higher MB dye concentration (>200 mg L^{-1}), the adsorption capacities displayed slightly noticeable enhancement which can be explained by the increasing repulsion forces between dye molecules on the surface of the adsorbent and the bulk phase following initial adsorption. Generally, the adsorption capacities of the MoS_2/ZIF-8 composite

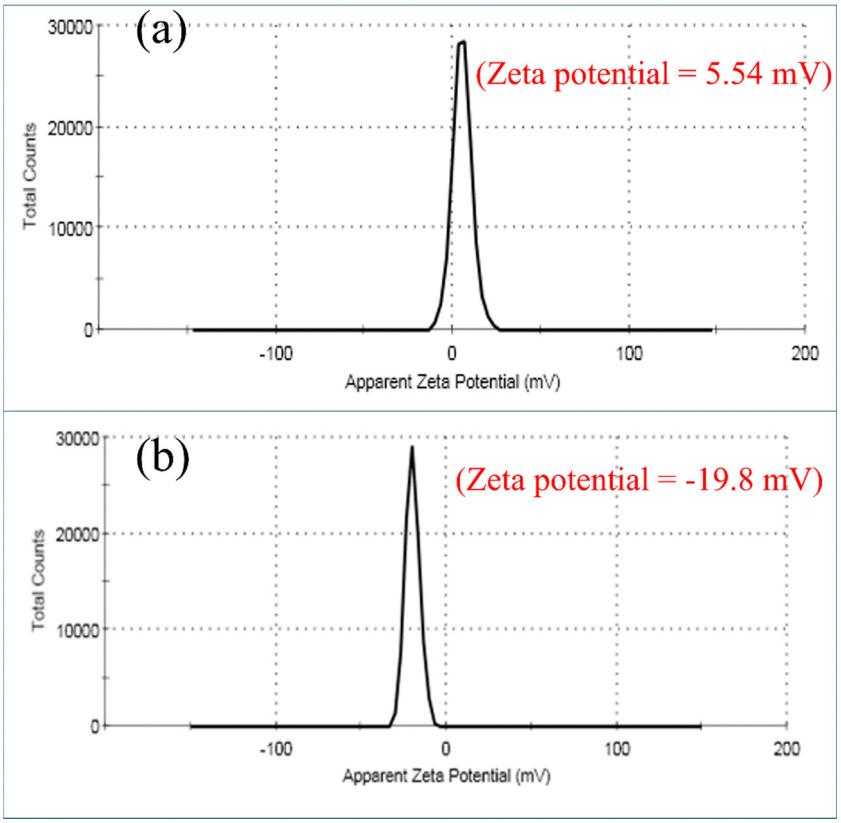

Fig. 5 Zeta potential the (a) ZIF-8 and (b) MoS_2/ZIF-8 composite before MB adsorption.

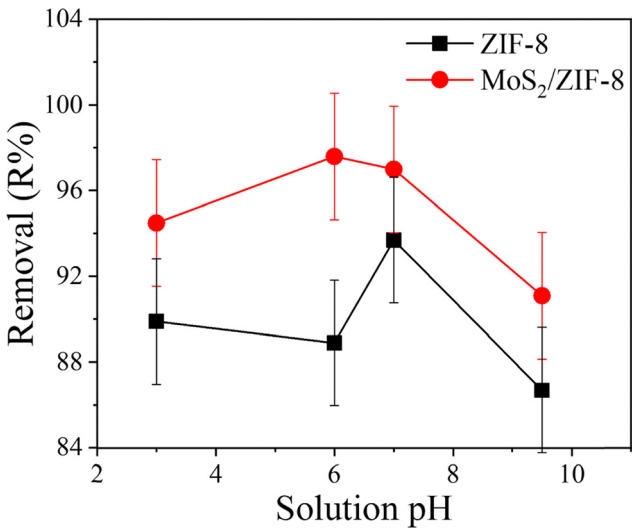

Fig. 6 Effect of pH on the MB removal from aqueous solution.

toward MB are higher than those achieved by ZIF-8, which can be ascribed to the increase in adsorption active sites by MoS_2, which is important for the adsorption.

3.3. Adsorption isotherms

Four different adsorption isotherm models were used in this study, Langmuir, Freundlich isotherms, Temkin, and Dubinin–Radushkevich (D–R). The isotherm plots are shown in Fig. 9, and the parameters are categorized in Table 1. The Langmuir isotherm is effective for monolayer adsorption on adsorbent surfaces with a limited number of indistinguishable sites.[62] According to this model, all the sites on the adsorbent surface are energetically equal. The Langmuir isotherm is represented by eqn (3).

$$\frac{C_e}{q_e} = \frac{C_e}{q_m} + \frac{1}{K_L q_m} \quad (3)$$

where C_e (mg L^{-1}) is an equilibrium concentration, q_e (mg g^{-1}) is the adsorption capacity at equilibrium, q_m (mg g^{-1}) is the maximum adsorbent capacity, C_0 (mg L^{-1}) is the initial concentration of the dye, and K_L (L mg^{-1}) is the Langmuir constant.

The reversible adsorption on different adsorption energy sites can be reported using the Freundlich isotherm model as an empirical equation. The Freundlich isotherm relates the quantity of solutes adsorbed (q_e) to the equilibrium concentration of solute in solution (C_e). The equation of Freundlich isotherm is stated as in eqn (4).

$$\log q_e = \log K_f + \frac{1}{n} \log C_e \quad (4)$$

where, n is the adsorption intensity which should have a value between 0.10 and 1.0 for favorable adsorption and K_f is a Freundlich constant.

Temkin isotherm describes the interaction between the adsorbent and adsorbate This isotherm is defined as follows.

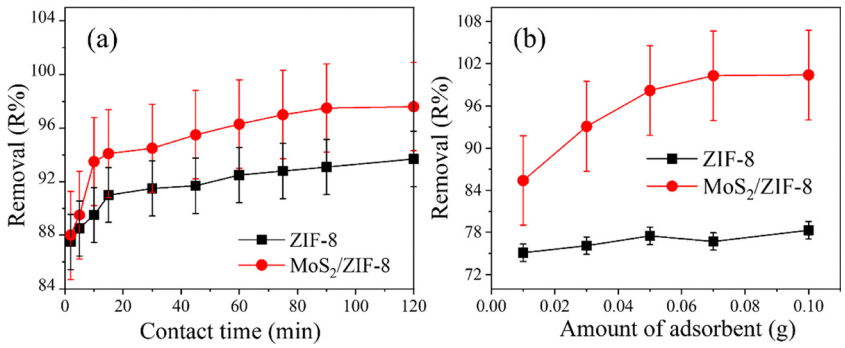

Fig. 7 Effect of (a) contact time and (b) adsorbent dose on removal efficiency.

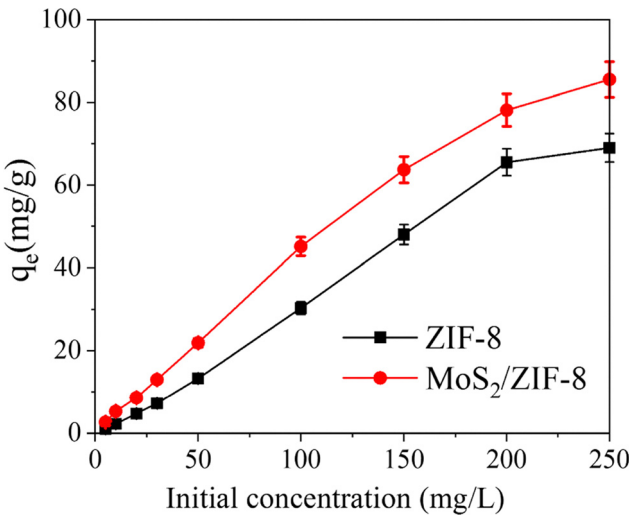

Fig. 8 Effect of initial concentration on removal from aqueous solution.

$$q_e = B\ln(C_e) + B\ln(K_T) \quad (5)$$

where B is a constant related to the heat of adsorption (J mol^{-1}). The B and K_T values were obtained from the plot of q_e *versus* ln C_e for the adsorbent.

The Dubinin–Radushkevich (D–R) isotherm model is employed for the differentiation of chemisorption and physisorption. The reason behind the development of several layers on microporous adsorbing materials can be understood through it. It is more general relative to the Langmuir model because it does not assume surface homogeneity.[63] Eqn (6) represents this model, where the gas constant R = 8.314 J mol^{-1} K^{-1}, and the absolute temperature is T (K).

$$\ln q_e = \ln q_m - \beta\varepsilon^2 \quad (6)$$

The Langmuir model exhibited the highest correlation coefficients (R^2 = 0.9777 for ZIF-8 and 0.9904 for MoS_2/ZIF-8), indicating that the adsorption process is monolayer coverage on a homogeneous surface. The maximum monolayer adsorption capacities were 19.61 mg g^{-1} for ZIF-8 and 88.03 mg g^{-1} for MoS_2/ZIF-8. The Freundlich model also provided a good fit (R^2 = 0.9704 and 0.9794), suggesting adsorption on a heterogeneous surface. The Freundlich constants ($n < 1$) indicate good adsorption conditions. The Temkin model showed moderate correlation (R^2 = 0.677 and 0.628), indicating a linear decrease in the heat of adsorption as surface coverage increases. The Temkin constant B values (27.34 and 26.35 kJ mol^{-1}) indicate that there is some degree of chemisorption involved in the process. Conversely, the D–R model presented relatively low correlation coefficients (R^2 = 0.531 and 0.614), indicating poor fitting to the experimental data. The average free energy values ($E < 8$ kJ mol^{-1}) confirm that the adsorption of MB dye on both ZIF-8 and MoS_2/ZIF-8 predominantly takes place *via* physisorption mechanisms governed by weak van der Waals interactions. Overall, the results indicate that the Langmuir model best explains the adsorption behavior, indicating monolayer adsorption on a homogeneous surface with dominating chemisorption nature, and the composite MoS_2/ZIF-8 shows superior adsorption performance compared to pristine ZIF-8.

3.4. Adsorption kinetics

The kinetic isotherm parameters for MB dye adsorption onto ZIF-8 and MoS_2/ZIF-8 were fitted with four common models: pseudo-first-order, pseudo-second-order, Weber–Morris intra-particle diffusion, and the Elovich model. Linear regression kinetic models were used. The pseudo-first-order model is represented by eqn (7) and the pseudo-second-order model is represented by eqn (8).[64]

$$\ln(q_e - q_t) = \ln q_e - K_1 t \quad (7)$$

$$\frac{t}{q_t} = \frac{t}{q_e} + \frac{1}{k_2 q e^2} \quad (8)$$

where q_e and q_t are the amounts of adsorbed dye in mg g^{-1} at equilibrium and time t, respectively. k_1 (min^{-1}) and k_2 (mg g^{-1} min^{-1}) are the pseudo-first and pseudo-second-order kinetic model, respectively.

The Weber–Morris intra-particle diffusion model was used to describe the diffusion mechanism and is expressed as follows.

$$q_t = k_3 t^{1/2} + C \quad (9)$$

where k_3 and C are the intra-particle diffusion rate constant (mg g^{-1} min$^{-1/2}$) and intercept, respectively.

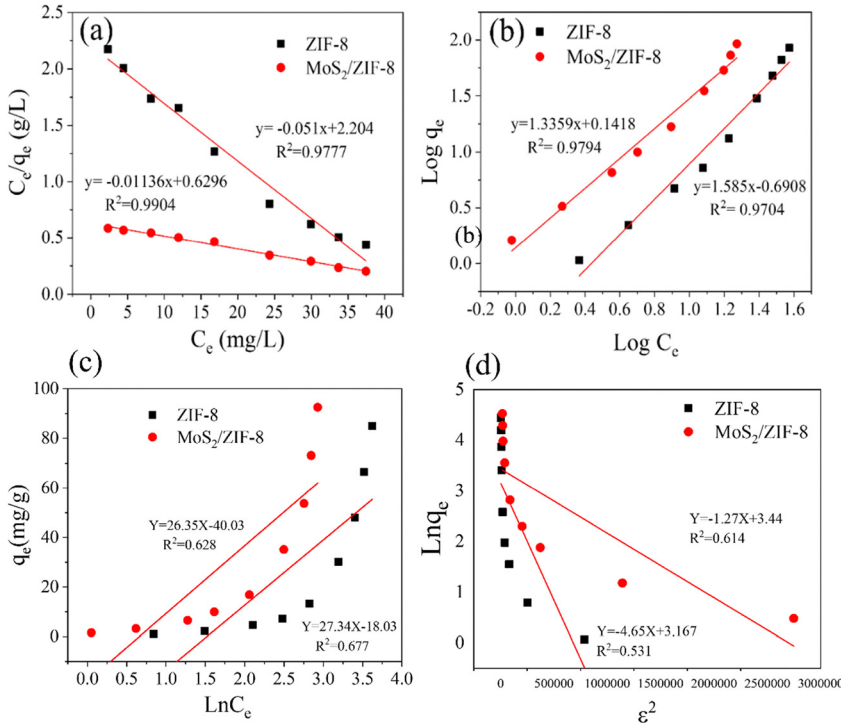

Fig. 9 Isotherm plots for the adsorption of MB onto ZIF-8 and the MoS_2/ZIF-8 composite: (a) Langmuir, (b) Freundlich, (c) Temkin, and (d) Dubinin–Radushkevich (D–R) isotherm models.

Table 1 Parameters of the isotherm models for the adsorption of MB on ZIF-8 and the MoS_2/ZIF-8 composite

Model	Parameter	ZIF-8	MoS_2/ZIF-8
Langmuir model	K_L (L mg^{-1})	0.023	0.018
	q_m (mg g^{-1})	19.61	88.03
	R^2	0.9777	0.9904
Freundlich model	K_f (mg g^{-1})	4.907	1.386
	n	0.631	0.748
	R^2	0.9704	0.9794
Temkin	B (kJ mol^{-1})	27.34	26.35
	K_T (L g^{-1})	0.522	0.219
	R^2	0.677	0.628
Dubinin–Radushkevich (D–R)	q_m (mg g^{-1})	23.74	31.19
	E (kJ mol^{-1})	0.627	0.33
	R^2	0.531	0.614

The Elovich kinetic model was used for the chemisorption of gases onto heterogeneous surfaces and solid systems and has also now found an application for the study of the removal of pollutants from aqueous solutions.[65] It describes the second-order kinetics assuming that the solid surface has heterogeneous energy but does not propose any mechanism for adsorption.[66] The Elovich model equation is generally expressed as eqn (10).

$$q_t = \frac{1}{\beta}\ln(\alpha\beta) + \frac{1}{\beta}\ln t \quad (10)$$

where q_t (mg g^{-1}) is the amount of adsorbate adsorbed at time t (min), α (mg g^{-1} min^{-1}) is the initial adsorption rate, and β (g mg^{-1}) is the desorption rate related to the extent of surface coverage and activation energy for chemisorption.

The fitting curves for the kinetic model are represented in Fig. 10(a–d), and their related parameters are presented in Table 2. Among the models, the pseudo-second-order model (Fig. 10b) provided the best description of the experimental data, as evidenced by the highest correlation coefficients (R^2 = 0.999 for both adsorbents). This indicates that chemisorption through valence forces by sharing or exchange of electrons between the adsorbent and dye molecules is the predominant process that controls the adsorption. The calculated equilibrium adsorption capacities obtained from the pseudo-second-order model (11.737 mg g^{-1} for ZIF-8 and 29.762 mg g^{-1} for MoS_2/ZIF-8) were in good agreement with the experimental values, confirming the validity of this kinetic model. The higher q_e value for MoS_2/ZIF-8 compared with ZIF-8 suggests that the incorporation of MoS_2 nanosheets enhances the number of available active sites and facilitates faster dye uptake.

The intra-particle diffusion plots (Fig. 10c) did not pass through the origin, indicating that intra-particle diffusion is not a rate-controlling step but occurs in parallel with adsorption on the surface.[67] The linearity for the Elovich model (Fig. 10d) was also satisfactory (R^2 = 0.98 and 0.951 for ZIF-8 and MoS_2/ZIF-8, respectively), indicating the chemisorption nature of the process. In addition, the higher value of initial adsorption rate (α) and lower value of desorption constant (β) for ZIF-8 compared to MoS_2/ZIF-8 are indicative of differences in surface energy distribution and adsorption site heterogeneity for the two materials. Accordingly, it is possible to conclude that the kinetics of MB dye adsorption onto ZIF-8 and MoS_2/ZIF-8 composites can be best described by the pseudo-second-

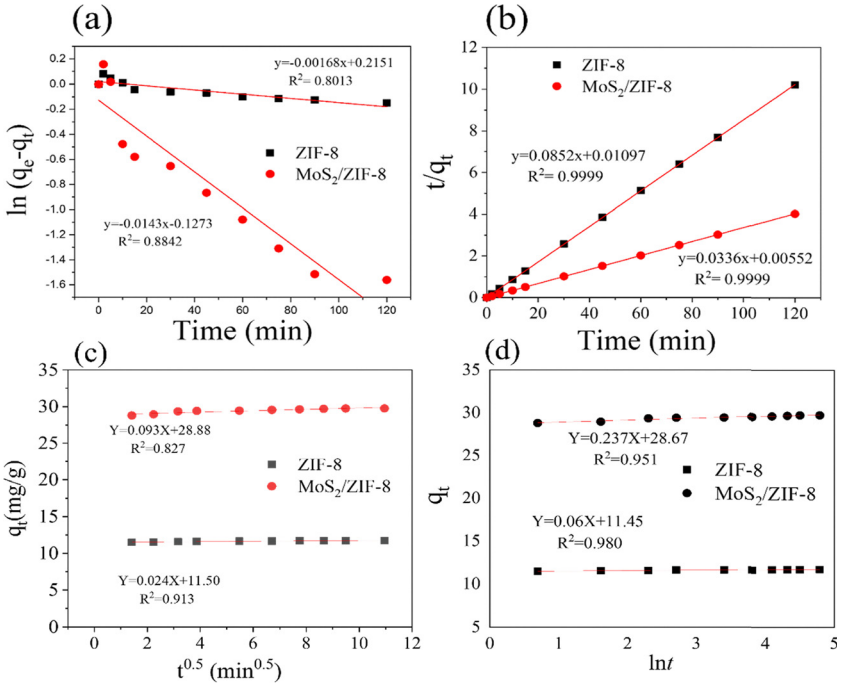

Fig. 10 The adsorption kinetics models fitting curves for the (a) pseudo first, (b) pseudo second order, (c) Weber–Morris intra-particle diffusion, and (d) Elovich kinetic models for the adsorption of MB by ZIF-8 and the MoS_2/ZIF-8 composite.

Table 2 Parameters of the kinetic models for the adsorption of MB on ZIF-8 and the MoS2/ZIF-8 composite

Model	Parameter	ZIF-8	MoS_2/ZIF-8
Pseudo-first-order	q_e (mg g^{-1})	1.240	1.136
	K_1 (1 min^{-1})	0.0017	0.014
	R^2	0.8013	0.8842
Pseudo second order	q_e (mg g^{-1})	11.737	29.762
	k_2 (mg g^{-1} min^{-1})	0.6617	0.2045
	R^2	0.999	0.999
Weber–Morris intra-particle diffusion	C	11.50	28.88
	k_3 (mg g^{-1} $min^{-1/2}$)	0.024	0.093
	R^2	0.913	0.827
Elovich	α (mg g^{-1} min^{-1})	1.136	0.315
	β (g mg^{-1})	16.666	4.219
	R^2	0.98	0.951

order model, which suggests that chemisorption is the dominant mechanism controlling the whole adsorption process.

3.5. Effects of temperature and thermodynamic analysis

Temperature plays a crucial role in determining the effect of adsorption with increasing temperature, as well as the ideal temperature for the ZIF-8/MoS_2 composite to remove MB. Equilibrium dye adsorption with an initial concentration of 30 mg L^{-1} and pH 7.2 in 40 mL containing 0.10 g for ZIF-8 and 0.04 g for the ZIF-8/MoS_2 composite within the temperature range of 30–70 °C was also determined on the same day. It investigated how temperature affected the ability of ZIF-8 and the MoS_2/ZIF-8 composite to remove MB dye. The equilibrium adsorption tests were carried out at five different temperatures between 30 and 70 °C. From results expressed in Fig. 11a, by raising the temperature from 30 to 70 °C, the removal efficiency of MB dye is enhanced which indicates that the adsorption is endothermic.[68] The thermodynamic behaviors for adsorption of MB over ZIF-8 and the MoS_2/ZIF-8 composite were investigated. Thermodynamic parameters such as Gibbs free energy, ΔG°, (kJ mol^{-1}), enthalpy change, ΔH°, (kJ mol^{-1}) and entropy change, ΔS°, (J K^{-1} mol^{-1}) were calculated using these equations (eqn (11)–(13)).[69]

$$\Delta G^\circ = -RT \ln K_L \quad (11)$$

$$\Delta G^\circ = \Delta H^\circ - T\Delta S^\circ \quad (12)$$

$$\ln K_L = -\left[\frac{\Delta H^\circ}{RT}\right] + \left[\frac{\Delta S^\circ}{R}\right] \quad (13)$$

where k_L is the adsorption distribution coefficient, T is the absolute temperature and R is the gas constant (8.314 J mol^{-1} K^{-1}).

From plots in Fig. 11b, values of ΔH° and ΔS° from the slope and intercept, respectively, on a Van't Hoff equation plot of

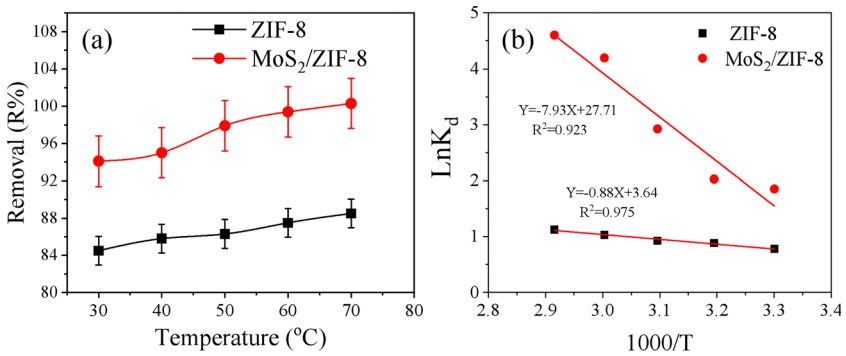

Fig. 11 (a) Effect of temperature on the removal of MB from aqueous solution and (b) Van't Hoff plots.

Table 3 Thermodynamic parameters for the adsorption of MB

			ΔG° (kJ mol^{-1})				
Adsorbents	ΔH° KJ mol^{-1}	ΔS° J mol^{-1} K^{-1}	303	313	323	333	343
ZIF-8	7.32	30.26	−9.16	−9.46	−9.77	−10.07	−10.37
MoS_2/ZIF-8	65.93	230.38	−69.74	−72.04	−74.35	−76.65	−78.95

ln K_L against $1/T$ where calculated, and then ΔG° was obtained. Table 3 summarizes all estimated thermodynamic parameters. Negative ΔG° values imply that adsorption was favorable and spontaneous. Positive values of ΔH° confirmed that the process was exothermic.[70] The positive entropy change (ΔS°) means that disorder increases during the process.

4. Reusability of adsorbent materials

The regeneration ability of ZIF-8 and MoS_2/ZIF-8 composites was examined through five successive adsorption–desorption cycles. The adsorbents were washed with distilled water and dried at 60 °C between each cycle to be reused. As in Fig. 12, both adsorbents exhibited satisfactory stability. The MoS_2/ZIF-8 composite maintained approximately 75% of its initial efficiency after five cycles, whereas approximately 56% was maintained by ZIF-8. The marginal decrease in performance was caused by partial pore blocking or incomplete desorption of the dye molecules.[28] These results bear witness to the excellent reusability and structural stability of the MoS_2/ZIF-8 composite for cyclic MB removal.

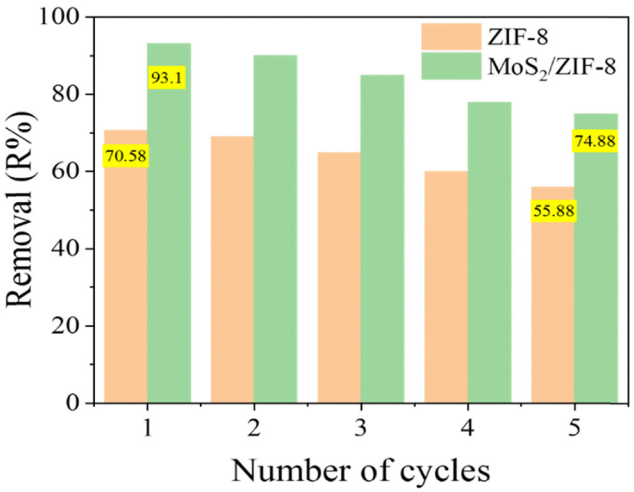

Fig. 12 The reusability of ZIF-8 and the MoS2/ZIF-8 composite toward MB adsorption.

4.1. Proposed mechanism of the interaction between MB dye and the MoS_2/ZIF-8 composite

The adsorption of MB dye onto the MoS_2/ZIF-8 composite is governed by a synergy of electrostatic attraction, chemisorption, and physisorption mechanisms. As determined by zeta potential measurement, MoS_2/ZIF-8 has a pH_pzc of 5.9, and the surface of the composite becomes negatively charged at pH > pH_pzc. Accordingly, at near-neutral pH, the negatively charged surface strongly attracts cationic MB^+ molecules *via* electrostatic interactions, which favors dye uptake. Adsorption isotherm studies indicate that the process is most adequately described by the Langmuir model with monolayer adsorption onto energetically homogeneous sites, and the Freundlich model indicates some heterogeneity and possible multilayer formation. The Temkin and D–R models suggest that the adsorption involves both chemisorptive (electron sharing or exchange) interactions and weak van der Waals forces, consistent with the pseudo-second-order kinetics indicated. The high R^2 values of this kinetic model imply that chemisorption is dominant, where valence forces facilitate binding of MB molecules onto active sites of the composite, *i.e.*, functional groups of MoS_2 and the ZIF-8 framework. Thermodynamic analysis indicates that the adsorption is spontaneous and endothermic, as evidenced by negative ΔG°, positive ΔH°, and positive ΔS°, implying higher disorder at the solid–liquid interface and higher adsorption at elevated temperatures. In addition, intraparticle diffusion is not the sole rate-controlling step; instead,

surface adsorption and micropore diffusion occur simultaneously. The incorporation of MoS_2 nanosheets introduces additional active sites and accessible surface area, leading to faster dye uptake and higher adsorption capacity compared to pristine ZIF-8.

5. Conclusion

Here, in this research study, ZIF-8 and MoS_2/ZIF-8 composite adsorbents were successfully examined as efficient adsorbents in the removal of methylene blue (MB) dye from aqueous solutions. The MoS_2/ZIF-8 composite exhibited much higher adsorption capacity (88.03 mg g^{-1}) than that of its pristine counterpart ZIF-8 (19.61 mg g^{-1}), emphasizing the synergistic effect of combining MoS_2 towards enhancing surface area, porosity, and accessibility of active sites. Adsorption equilibrium values were best described by the Langmuir isotherm, implying monolayer adsorption on a uniform surface, while kinetic measurements obeyed the pseudo-second-order model, which supports that chemisorption *via* electron sharing or exchange predominates in the process. Thermodynamic analysis found MB adsorption to be spontaneous, endothermic, and with increased randomness at the solid–liquid interface. Mechanistic investigations showed that the adsorption involves electrostatic attraction, chemisorption at active sites, and physisorption *via* van der Waals forces, and intra-particle diffusion occurring concurrently with surface adsorption. Overall, the MoS_2/ZIF-8 composite shows good performance and great potential as a reusable and efficient adsorbent for the removal of cationic dye-contaminated wastewater.

Author contributions

Rofaida. F. H. Darweesh: performed the experimental work and writing – original draft. Remon. M. Zaki: review and supervision. Aldoshy. Mahdy: supervision. Abdelaal S. A. Ahmed: writing – review & editing and supervision. The manuscript was reviewed by all the authors before publication.

Conflicts of interest

The authors declare that 'There are no conflicts to declare'.

Data availability

In this study, we have included all data in the main manuscript, and we have no other data available.

References

1 L. Yang, L. Bao, Y. Zhong, C. Hao, J. Chen, J. Wu and X. Wang, *J. Cleaner Prod.*, 2024, **434**, 139831.
2 M. E. Mostafa, H. Mohamed, A. M. Kamal El-Dean, R. M. Zaki and M. Abdel-Mogib, *Egypt. Sugar J.*, 2020, **14**, 37–50.
3 R. Foroutan, S. J. Peighambardoust, S. Ghojavand, M. Foroughi, A. Ahmadi, F. Bahador and B. Ramavandi, *Biomass Convers. Biorefin.*, 2024, **14**, 25685–25700.
4 A. S. A. Ahmed, M. M. S. Sanad, A. Kotb, A. N. R. M. Negm and M. H. Abdallah, *Mater. Adv.*, 2023, **4**, 2981–2990.
5 L. Li, Y. Zhong, Y. Hu, J. Bai, F. Qiao, A. S. A. Ahmed, G. Ali, X. Zhao and Y. Xie, *CrystEngComm*, 2023, **25**, 4355–4363.
6 H. Fan, J. Gu, H. Meng, A. Knebel and J. Caro, *Angew. Chem., Int. Ed.*, 2018, **57**, 4083–4087.
7 A. Yanyan, Z. Huaili, Y. Zhishuang, S. Yongjun, W. Yili, Z. Chun and D. Wei, *J. Hazard. Mater.*, 2020, **381**, 120971.
8 D. Tolan, A. El-Sawaf, A. S. A. Ahmed, A. Nassar, N. M. Mohamed, I. G. Alhindawy, E. A. Elshehy and V. Utgikar, *Mater. Chem. Phys.*, 2024, **322**, 129570.
9 E. H. Kaoutar, K. Daina, T. Maris, B. Buscotin Horax and A. Abdellah, *Sep. Purif. Technol.*, 2019, **210**, 764–774.
10 N. S. M. Sayed, A. S. A. Ahmed, M. H. Abdallah and G. A. Gouda, *Sci. Rep.*, 2024, **14**, 5384.
11 Y. Chu, S. Zhu, F. Wang, W. Lei, M. Xia and C. Liao, *J. Chem. Eng. Data*, 2019, **64**, 3535–3546.
12 B. Thomas, E. P. Shilpa and L. K. Alexander, *Emergent Mater.*, 2021, **4**, 1479–1487.
13 Y. Chu, M. A. Khan, M. Xia, W. Lei, F. Wang and S. Zhu, *J. Chem. Eng. Data*, 2019, **64**, 5900–5909.
14 N. U. M. Nizam, M. M. Hanafiah, E. Mahmoudi, A. A. Halim and A. W. Mohammad, *Sci. Rep.*, 2021, **11**, 8623.
15 M. H. E. Mohamed, M. Taha and H. M. Abdelbary, *Al-Azhar Bull. Sci.*, 2023, 34.
16 Y.-Y. Li, Y.-L. Wu, N. Chen, Y.-L. Ma, W.-X. Ji and Y.-G. Sun, *Chin. J. Anal. Chem.*, 2023, **51**, 100278.
17 A. Alhujaily, H. Yu, X. Zhang and F. Ma, *Appl. Water Sci.*, 2020, **10**, 183.
18 H. Furukawa, K. E. Cordova, M. O'Keeffe and O. M. Yaghi, *Science*, 2013, **341**, 1230444.
19 D. Zhao, X. Wang, L. Yue, Y. He and B. Chen, *Chem. Commun.*, 2022, **58**, 11059–11078.
20 J. W. Maina, C. Pozo-Gonzalo, L. Kong, J. Schütz, M. Hill and L. F. Dumée, *Mater. Horiz.*, 2017, **4**, 345–361.
21 A. S. A. Ahmed, W. Xiang, I. Saana Amiinu and X. Zhao, *New J. Chem.*, 2018, **42**, 17303–17310.
22 A. S. A. Ahmed, W. Xiang, F. Shui, B. Li, H. H. A. Younes, I. S. Amiinu and X. Zhao, *Sol. Energy*, 2021, **218**, 117–128.
23 H. Kaur, N. Devi, S. S. Siwal, W. F. Alsanie, M. K. Thakur and V. K. Thakur, *ACS Omega*, 2023, **8**, 9004–9030.
24 X. Dong, Y. Lin, Y. Ma and L. Zhao, *RSC Adv.*, 2019, **9**, 27674–27683.
25 B. Luan Tran, H.-Y. Chin, B. K. Chang and A. S. T. Chiang, *Microporous Mesoporous Mater.*, 2019, **277**, 149–153.
26 X. Tong, J. Zhang, Q. Chen and H. Liu, *New J. Chem.*, 2021, **45**, 19416–19424.
27 S. R. A. Younis, M. Abdelmotallieb and A. S. A. Ahmed, *RSC Adv.*, 2025, **15**, 8594–8608.
28 A. S. A. Ahmed, E. S. A. Haggag, M. F. Cheira, A. A. Abdelsamad and A. M. Abdel-lateef, *RSC Adv.*, 2025, **15**, 36365–36379.
29 R. S. El Shenawy, A. F. Hassan and E. A. El Fadaly, *Int. J. Biol. Macromol.*, 2025, **322**, 146995.

30 M. A. Nazir, T. Najam, K. Shahzad, M. A. Wattoo, T. Hussain, M. K. Tufail, S. S. A. Shah and A. u Rehman, *Surf. Interfaces*, 2022, **34**, 102324.
31 Y. Li, P. Xiang, H. Chen and Y. Zhou, *J. Solid State Chem.*, 2022, **315**, 123538.
32 D. Tuncel and A. N. Ökte, *Catal. Today*, 2021, **361**, 191–197.
33 A. S. A. Ahmed, E. A. Elshehy and M. F. Cheira, in *Functionalization of Two-Dimensional Materials and Their Applications*, ed. W. A. El-Said and N. Ghany, Woodhead Publishing, 2024, pp. 115–149, DOI: 10.1016/B978-0-323-89955-0.00008-X.
34 I. S. Amiinu, Z. Pu, X. Liu, K. A. Owusu, H. G. R. Monestel, F. O. Boakye, H. Zhang and S. Mu, *Adv. Funct. Mater.*, 2017, **27**, 1702300.
35 J. Zhang, T. Wang, D. Pohl, B. Rellinghaus, R. Dong, S. Liu, X. Zhuang and X. Feng, *Angew. Chem., Int. Ed.*, 2016, **55**, 6702–6707.
36 M. Al-Mamun, H. Zhang, P. Liu, Y. Wang, J. Cao and H. Zhao, *RSC Adv.*, 2014, **4**, 21277.
37 C.-J. L. Sheng-Yen Tai, S.-W. Chou, F. S.-S. Chien, J.-Y. Lin and T.-W. Lin, *J. Mater. Chem.*, 2012, **22**, 24753–24759.
38 G. R. L. a X. P. G. B. Lei, *J. Mater. Chem. A*, 2014, **2**, 3919–3925.
39 Z. Ying, L. Huang, L. Ji, H. Li, X. Liu, C. Zhang, J. Zhang and G. Yi, *Materials*, 2021, **14**(7), 1754.
40 A. M. E. Mohammed, A. Kotb, M. M. S. Sanad, M. Abdel-Hakim and A. S. A. Ahmed, *RSC Adv.*, 2024, **14**, 31332–31347.
41 J. Zhou, M. Li, Y. Tao and L. Zha, *Molecules*, 2025, **30**(5), 992.
42 A. El-Sawaf, D. A. Tolan, M. S. Abdelrahman, I. A. El-Hay, M. Ismael, A. S. A. Ahmed, E. A. Elshehy and M. T. Abdu, *J. Chem. Technol. Biotechnol.*, 2024, **99**, 1941–1954.
43 H. A. Abdelmonem, T. F. Hassanein, H. E. Sharafeldin, H. Gomaa, A. S. A. Ahmed, A. M. Abdel-lateef, E. M. Allam, M. F. Cheira, M. E. Eissa and A. H. Tilp, *Colloids Surf., A*, 2024, **684**, 133081.
44 Ü. Bayram, Ç. Özer and E. Yilmaz, *ACS Omega*, 2025, **10**, 9986–10003.
45 J. Tang, R. R. Salunkhe, J. Liu, N. L. Torad, M. Imura, S. Furukawa and Y. Yamauchi, *J. Am. Chem. Soc.*, 2015, **137**, 1572–1580.
46 W.-Q. Chen, L.-Y. Li, L. Li, W.-H. Qiu, L. Tang, L. Xu, K.-J. Xu and M.-H. Wu, *Engineering*, 2019, **5**, 755–767.
47 H. S. Matte, A. Gomathi, A. K. Manna, D. J. Late, R. Datta, S. K. Pati and C. N. Rao, *Angew. Chem., Int. Ed.*, 2010, **49**, 4059–4062.
48 X. Zheng, J. Xu, K. Yan, H. Wang, Z. Wang and S. Yang, *Chem. Mater.*, 2014, **26**, 2344–2353.
49 Y. Hu, H. Kazemian, S. Rohani, Y. Huang and Y. Song, *Chem. Commun.*, 2011, **47**, 12694–12696.
50 Y. Hu, Z. Liu, J. Xu, Y. Huang and Y. Song, *J. Am. Chem. Soc.*, 2013, **135**, 9287–9290.
51 J. Shen, A. Liu, Y. Tu, G. Foo, C. Yeo, M. B. Chan-Park, R. Jiang and Y. Chen, *Energy Environ. Sci.*, 2011, **4**, 4220–4229.
52 M. A. Lukowski, A. S. Daniel, F. Meng, A. Forticaux, L. Li and S. Jin, *J. Am. Chem. Soc.*, 2013, **135**(28), 10274–10277.
53 F. Azeez, E. Al-Hetlani, M. Arafa, Y. Abdelmonem, A. A. Nazeer, M. O. Amin and M. Madkour, *Sci. Rep.*, 2018, **8**, 7104.
54 J. Chen, X. Wang, Y. Huang, S. Lv, X. Cao, J. Yun and D. Cao, *Eng. Sci.*, 2019, **5**, 30–38.
55 J. J. Salazar-Rabago, R. Leyva-Ramos, J. Rivera-Utrilla, R. Ocampo-Perez and F. J. Cerino-Cordova, *Sustainable Environ. Res.*, 2017, **27**, 32–40.
56 Y. Liu, C. Luo, J. Sun, H. Li, Z. Sun and S. Yan, *J. Mater. Chem. A*, 2015, **3**, 5674–5682.
57 W. A. Shaltout, A. F. Hassan, M. S. Elsayed and H. Hafez, *Mater. Adv.*, 2025, **6**, 4418–4437.
58 S. J. Olusegun and N. D. S. Mohallem, *Environ. Pollut.*, 2020, **260**, 114019.
59 T. Maneerung, J. Liew, Y. Dai, S. Kawi, C. Chong and C. H. Wang, *Bioresour. Technol.*, 2016, **200**, 350–359.
60 K. Mensah, H. Mahmoud, M. Fujii, M. Samy and H. Shokry, *Bio. Conver. Biorefinery*, 2022, **14**, 12945–12960.
61 S. Hassan, E. Marwa and H. Hesham, *J. Mater. Res. Technol.*, 2019, **8**, 4477–4488.
62 I. Langmuir, *J. Am. Chem. Soc.*, 1918, **40**, 1361–1403.
63 A. E. Mohammed, N. F. Al-Harby, M. Alrasheedi, S. M. Ibrahim and N. A. Mohamed, *Inorganics*, 2025, **13**(4), 116.
64 A. El-Sawaf, D. A. Tolan, M. S. Abdelrahman, I. A. El-Hay, M. Ismael, A. S. A. Ahmed, E. A. Elshehy and M. T. Abdu, *J. Chem. Technol. Biotechnol.*, 2024, **99**, 1941–1954.
65 A. B. Al-Odayni, F. S. Alsubaie, N. A. Y. Abdu, H. M. Al-Kahtani and W. S. Saeed, *Polymers*, 2023, 15.
66 U. A. Edet and A. O. Ifelebuegu, *Processes*, 2020, **8**(6), 665.
67 K. H. Chu, M. A. Hashim, M. H. Zawawi and J.-C. Bollinger, *J. Environ. Chem. Eng.*, 2025, **13**, 117266.
68 R. H. Althomali, K. A. Alamry, M. A. Hussein and R. M. Guedes, *RSC Adv.*, 2023, **13**, 4303–4313.
69 A. F. Hassan, A. F. El-kott, M. A. AlShehri and F. M. Aldosari, *Water, Air, Soil Pollut.*, 2025, **236**, 491.
70 E. J. E. Abdelrazek, A. A. Gahlan, G. A. Gouda and A. S. A. Ahmed, *Sci. Rep.*, 2025, **15**, 4123.